Electronic Supplementary Information for

Prominent Electronic Effect in Iridium-Alloy-Skinned Nickel Nanoparticles Boosts Alkaline Hydrogen Electrocatalysis

Jie Xu[a,d‡], Xuyan Wang[a,b‡], Xinnan Mao[a,b‡], Kun Feng[a,b], Jiabin Xu[a,b], Jun Zhong[a,b*], Lu Wang[a,b*], Na Han[a,b*] and Yanguang Li[a,b,c*]

[a] Institute of Functional Nano & Soft Materials (FUNSOM), Soochow University, Suzhou, 215123 China

[b] Jiangsu Key Laboratory for Advanced Negative Carbon Technologies, Soochow University, Suzhou 215123, China

[c] Macao Institute of Materials Science and Engineering (MIMSE), MUST-SUDA Joint Research Center for Advanced Functional Materials, Macau University of Science and Technology, Taipa 999078, Macau SAR, China

[d] College of Chemistry and Materials Engineering, Wenzhou University, Wenzhou, Zhejiang 325035, China

‡ These authors contributed equally.

Correspondence to: yanguang@suda.edu.cn, hanna@suda.edu.cn, lwang22@suda.edu.cn, jzhong@suda.edu.cn

Experimental section

Chemicals and materials.

All reagents are analytical grade and used as received without further purification. Nickel(II) acetylacetonate ($Ni(acac)_2$, 95%) and iridium(III) acetylacetonate ($Ir(acac)_3$, Ir 37.5% min) were purchased from Alfa Aesar. Oleylamine (OAm, C18: 80–90%) was purchased from Shanghai Macklin Biochemical Co., Ltd. Cyclohexane (≥99.7%) was purchased from Sinopharm Chemical Reagent Co., Ltd. Ketjenblack conductive carbon black (KB, Carbon ECP 200L) was purchased from Lion Specialty Chemicals Co., Ltd. Commercial PtRu/C (20 wt% platinum and ruthenium on Vulcan XC72), Pt/C (20 wt% platinum on Vulcan XC72) and Ir/C (20 wt% iridium on Vulcan XC72) were purchased from Premetek Co. Perfluorinated resin solution (Nafion 1100EW, 5 wt. % in lower aliphatic alcohols and water, contains 15-20% water) was purchased from Sigma-Aldrich. Deionized water was prepared with a Milli-Q purification system and used throughout all the experiments.

Material synthesis

Preparation of Ni@IrNi

To prepare Ni@IrNi, 20 mg of $Ni(acac)_2$ and 7 mg of $Ir(acac)_3$ were first dissolved in 15 mL of oleylamine and vigorously stirred for 30 min. The solution was transferred into a 25 mL autoclave, and heated at 200°C for 24 h in an oven. The obtained product was isolated, washed by ethanol and mixed with a calculated amount of KB in cyclohexane. The mixture was then washed thoroughly with ethanol and water, and finally lyophilized to yield the named product. Pure Ni nanoparticles, Ni@IrNi-1 and Ni@IrNi-3 were prepared by changing the $Ir(acac)_3$ precursor mass to 0 mg, 3 mg,

10 mg, respectively under otherwise identical conditions. To etch its metallic Ni cores, Ni@IrNi was soaked in 10 wt% HCl for 12 h, and washed with distilled water to afford e-Ni@IrNi for control experiments.

Structure characterizations

Powder XRD was conducted on a PANalytical X-ray diffractometer. TEM/HAADF imaging and EDS mapping were carried out on a Thermo Scientific Talos F200X scanning/transmission electron microscope under 200 kV. XPS results were obtained on a Thermo Scientific K-Alpha X-ray photoelectron spectrometer. X-ray absorption spectroscopy (XAS) experiments were performed at the Shanghai Synchrotron Radiation Facility (SSRF, 14W). Ir L_3-edge XANES and EXAFS spectra were collected from ~200 eV below to ~800 eV above the Ir L_3-edge in the transmission mode. Ni K-edge XANES and EXAFS spectra were collected from ~200 eV below to ~800 eV above the Ni K-edge in the transmission mode. ICP results were analyzed using an Aurora M90 inductively coupled plasma optical emission spectrometer.

Electrochemical measurements

All the electrochemical experiments were conducted using a three-electrode cell system with a glassy carbon rotating disk electrode (RDE, Pine Instruments) as the working electrode, a saturated calomel electrode (SCE) as the reference electrode, and a graphite rod as the counter electrode. All the potentials were referenced to the reversible hydrogen electrode (RHE) and compensated for iR drop. For the preparation of the working electrode,1 mg of Ni@IrNi, 500 μL of ethanol and 7 μL of 5 wt%

Nafion solution were mixed and sonicated for 1 h to form a homogeneous catalyst ink. Then, 5 μL of ink was dropcast onto the pre-polished RDE to form a smooth catalyst film with an Ir loading of 6.25 μg cm^{-2}. To further lower the catalyst loading, 1 mg of Ni@IrNi, 2 mg of KB, 1000 μL of ethanol, and 8 μL of 5 wt% Nafion solution were mixed and sonicated, and 4 μL of the catalyst ink was dropcast onto the RDE. For reference samples, 1 mg of 20 wt% Pt/C, 20 wt% Ir/C or 20 wt% PtRu/C was dispersed in 500 μL of ethanol and 6 μL of 5 wt% Nafion solution. After sonicated for 1 h, 5 μL of the ink was dropcast onto the RDE to achieve a metal loading of 10 μg cm^{-2}.

The electrochemical HOR/HER tests were carried out in a H_2-saturated 0.1 M/1 M KOH or 0.1 M PBS electrolyte. Prior to measurements, the electrolyte was bubbled with 99.999% H_2 for 40 min to reach its saturation. The bubbling continued during HOR and HER measurements. HOR polarization curves were collected at different electrode rotating speeds with a scan rate of 5 mV s^{-1}. HER polarization curves were collected at 1600 rpm with a scan rate of 10 mV s^{-1}.

The kinetic current density (j_k) was obtained via the Koutecky–Levich (K–L) equation:

$$\frac{1}{j}=\frac{1}{j_k}+\frac{1}{j_d}=\frac{1}{j_k}+\frac{1}{BC_0\omega^{1/2}}$$

where j is the measured current density which can be deconvoluted into j_k and diffusion limited current density (j_d) components, B is the Levich constant, C_0 is the solubility of H_2 in the electrolyte, and ω is the angular velocity of the rotating disk electrode. By plotting j^{-1} with respect to $\omega^{-1/2}$, and extrapolating the linear fitting to $\omega^{-1/2} = 0$, we derived j_k at η = 50 mV as described in our main text. The exchange current density (j_0) was calculated from the linear fitting of the micro-polarization region, where j could be approximated as j_k:

$$j = j_k = j_0\frac{\eta F}{RT}$$

where η is the overpotential, F is the Faraday's constant (96485 C mol^{-1}), R is the universal gas constant (8.314 J mol^{-1} K^{-1}), and T is the operating temperature (300 K).

Computational methods

All the DFT calculations were performed using the revised Perdew-Burke-Ernzerhof functionals (RPBE) of generalized gradient approximation (GGA) implemented in the Vienna Ab-initio Simulation Package (VASP) code (*Phys. Rev. B* **1999**, *59*, 7413; *Phys. Rev. B* **1996**, *54*, 11169; *Comput. Mater. Sci.* **1996**, *6*, 15). The projector-augmented wave (PAW) method was applied to describe the electron-ion interactions (*Phys. Rev. B* **1993**, *47*, 558; *Phys. Rev. B* **1994**, *50*, 17953). A kinetic energy cutoff for the plane wave expansions was set to be 400 eV. The method of Methfessel-Paxton (MP) was applied, and the width of the smearing was chosen as 0.2 eV. A 3 × 3 supercell with four atomic layers was used to construct the Ni (111) surface and Ir (111) surface. Two bottom layers were fixed at their bulk lattice parameters. In the first layer of Ni (111), six Ni atoms were replaced by Ir to model Ni@IrNi with the IrNi alloy surface. More than 10 Å of vacuum space was used to avoid the interaction of the adjacent images. We applied an additional dipole correction along the *z*-axis to remove spurious energy contributions arising from the asymmetric slab model. For sampling the reciprocal space, ***k***-points of Γ-centered 4 × 4 × 1 and 3 × 3 × 1 were used for the calculation of Ni@IrNi and Ir (111), respectively. To simulate the gaseous molecules, electronic structure calculations were performed in a 15 Å × 15 Å × 15 Å vacuum box with a Fermi smearing of 0.05 eV. The Γ-point was adopted for sampling the Brillouin zone of the simulation cell. All the structures were fully relaxed until all the forces were less than 0.03 $eV \cdot Å^{-1}$.

We employed the double-reference method to evaluate the influence of solvation and pH on the reaction energetics (*ACS Catal.* **2019**, *9*, 5567; *J. Phys. Chem. C* **2020**, *124*, 12016; *ACS Catal.* **2020**, *10*, 12148). It was modeled as implemented by the Hennig group in the VASPsol code (*J. Chem. Phys.* **2014**, *140*, 084106; J. Chem. Phys. **2019**, *151*, 234101). The relative permittivity of the electrolyte was set to be 78.36 (the dielectric constant of water at T = 298.15 K). A Debye screening length of 9.61 Å was chosen, corresponding to a bulk ion concentration of 0.1 M KOH at T = 298.15 K. The cavity setting in VASPsol was turned off to avoid numerical instabilities (*ACS Catal.* **2019**, *9*, 920). The electric potential of the slab referenced to the standard hydrogen electrode (SHE) was calculated as:

$$U_{\mathrm{SHE}}/\mathrm{V} = -4.60 - \varphi_q/\mathrm{eV}$$

where φ_q is the work function of the charged slab in the aqueous solution, and 4.60 V is the work function of the H_2/H^+ couple at standard conditions. At a constant U_{RHE}, when the pH is varied by one unit, the U_{SHE} is shifted by 0.059 V. Thus, an electrode at pH = 13 and U_{RHE} = 0 V has a U_{SHE} = -0.769 V. The calculated electronic energy (E_{elec}) of the charged system was then corrected for the interaction with the background charge as well as for the difference in the number of electrons in the system. For each structure, calculations were performed at charges of -0.500 |e| to +0.500 |e| with steps of +0.125 |e|. The electronic energy at the 9 charge values was then fit using a quadratic function to provide the electronic energy as a continuous function of U_{SHE}.

Finally, the calculated electronic energies were converted into free energies (G), by adding zero-point energies (ZPE), and enthalpic (H) and entropic (S) contributions of adsorbates obtained from a harmonic oscillator at T = 298.15 K. Free energy corrections for gaseous molecules were obtained

from the ideal gas approximation at T = 298.15 K (Table S4). The computational hydrogen electrode (CHE) model was applied to calculate the free energy change (ΔG) of electrochemical steps in the RHE scale (*J. Phys. Chem. B* **2004**, *108*, 17886).

The occupied *d*-band center was calculated using the following equation:

$$\varepsilon_d^T = \frac{\int_{-\infty}^{E_F} E\rho_d(E)dE}{\int_{-\infty}^{E_F} \rho_d(E)dE}$$

where E is the energy relative to the Fermi level, and $\rho_d(E)$ is the partial density of states projected

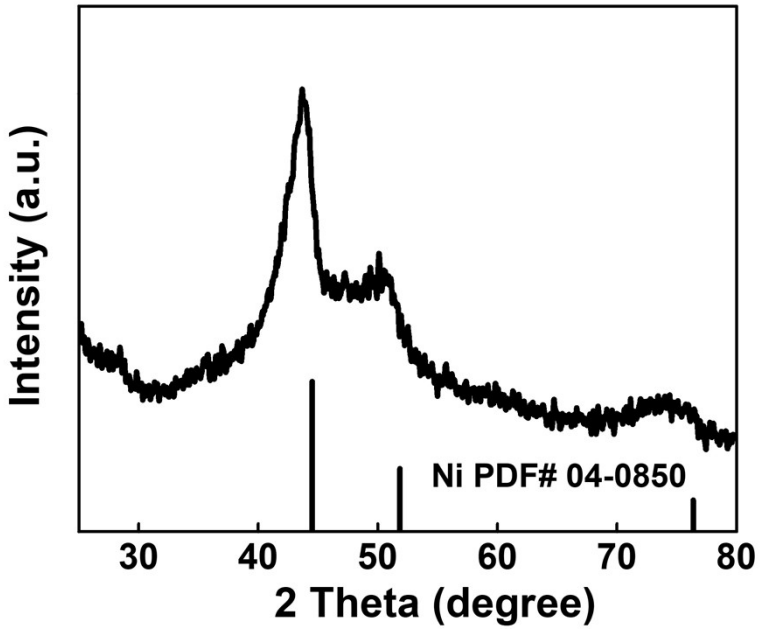

Fig. S1 XRD pattern of Ni@IrNi.

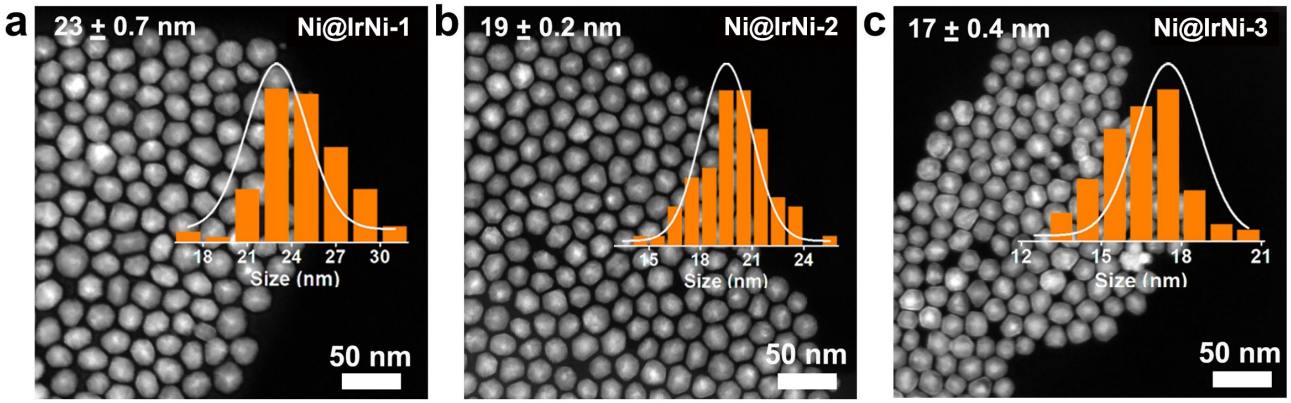

Fig. S2 HAADF images of (a) Ni@IrNi-1, (b) Ni@IrNi-2 and (c) Ni@IrNi-3, the insets are the corresponding particle size distribution.

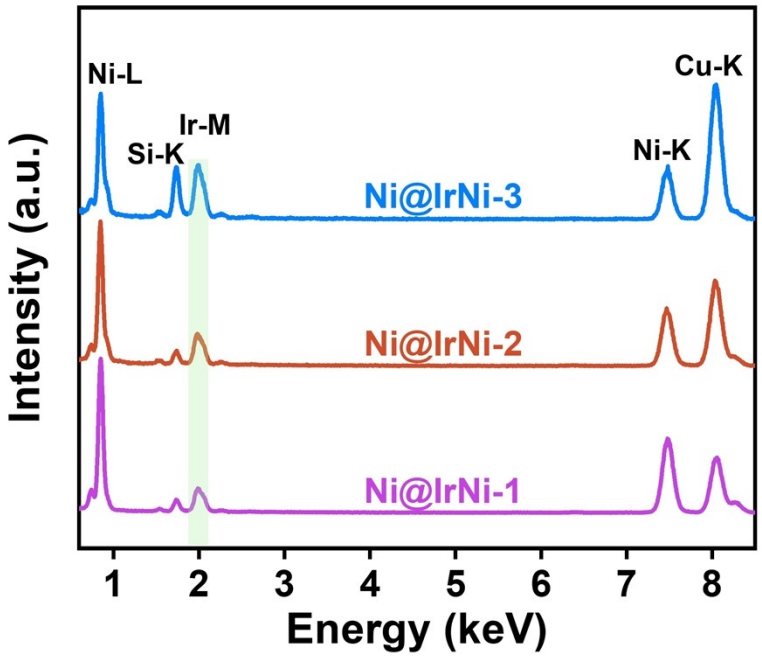

Fig. S3 EDS spectra of Ni@IrNi-1, Ni@IrNi-2 and Ni@IrNi-3, the Si and Cu signals are from the Cu grid.

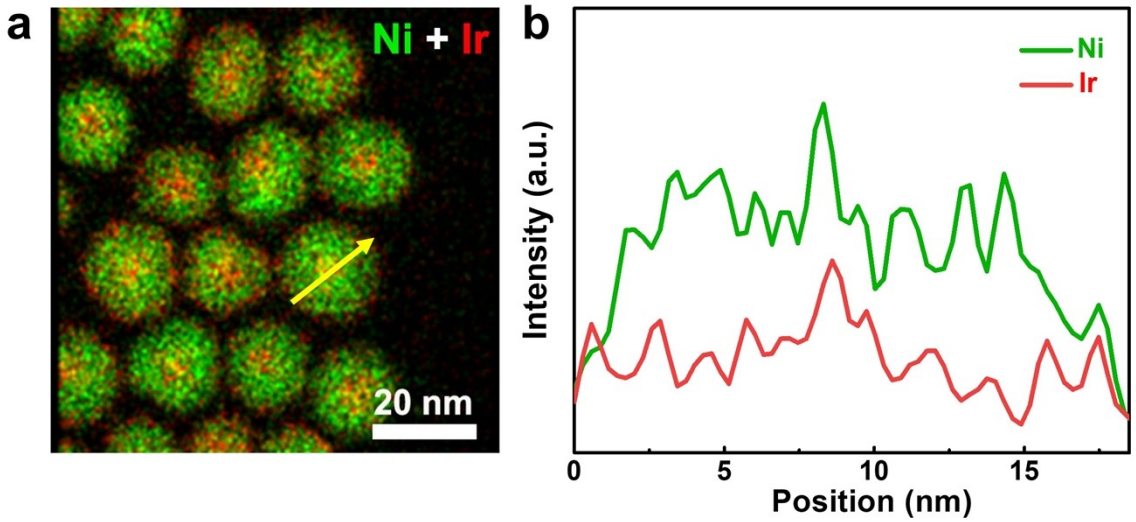

Fig. S4 (a) EDS mapping of Ni@IrNi; (b) EDS elemental line profiles along the yellow arrow in (a)

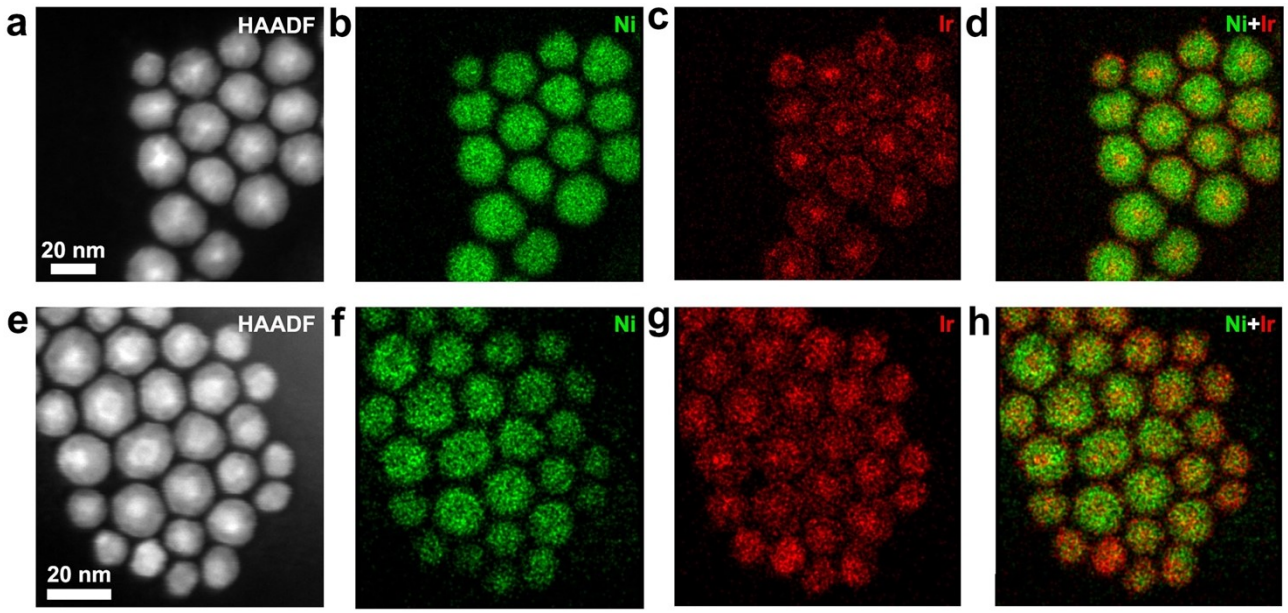

Fig. S5 EDS elemental mapping of Ni and Ir in (a-d) Ni@IrNi-1 and (e-h) Ni@IrNi-3.

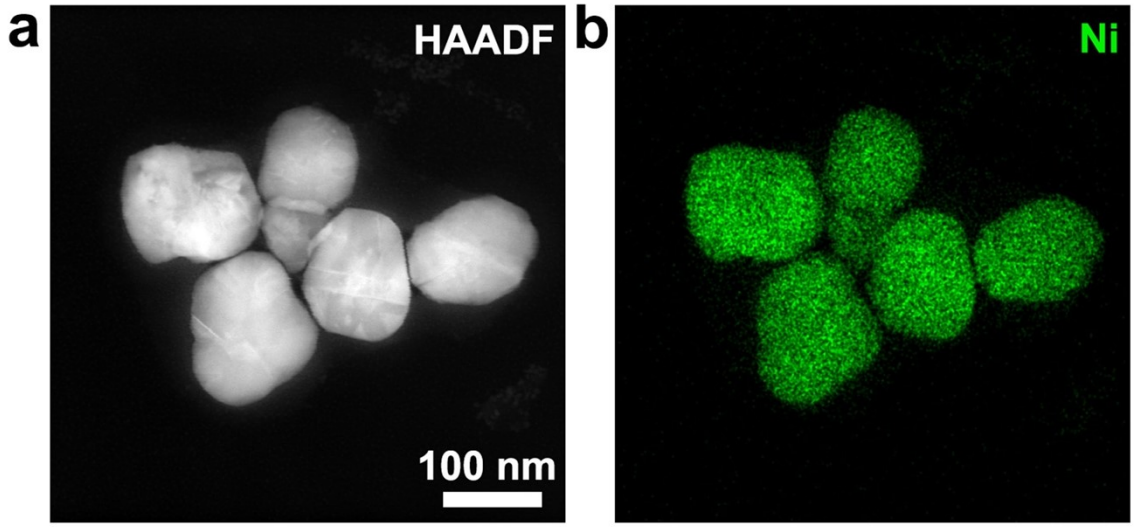

Fig. S6 (a) HAADF image and (b) EDS elemental mapping of Ni nanoparticles.

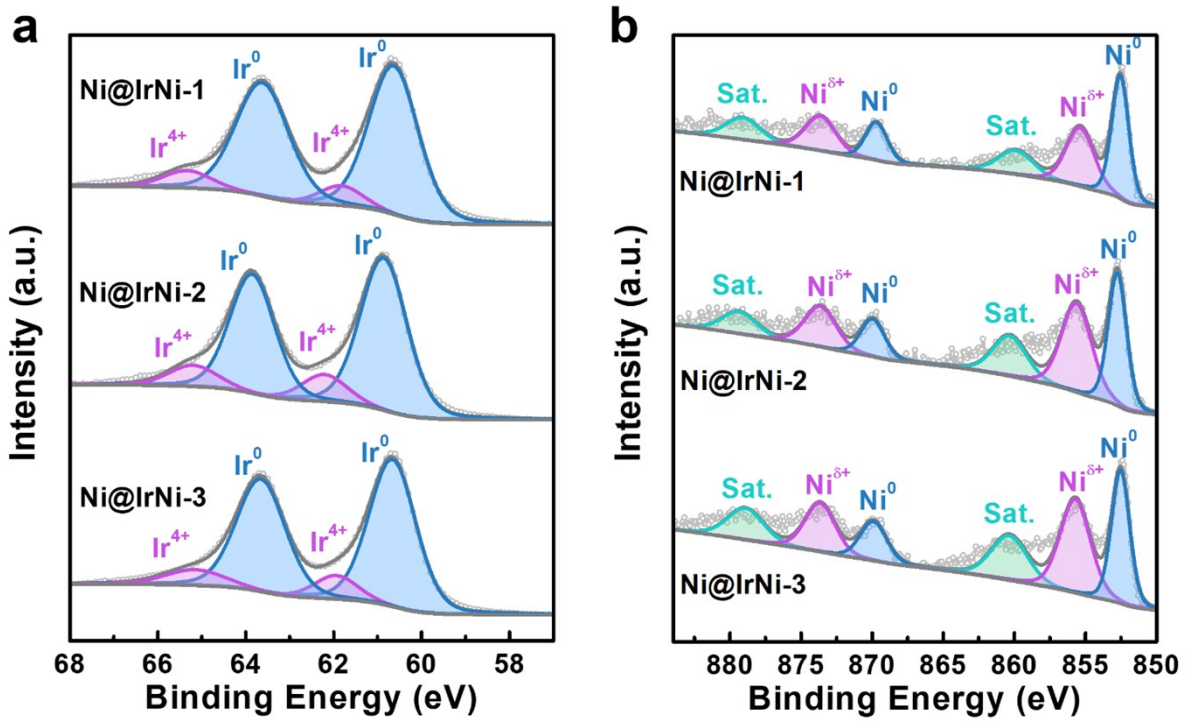

Fig. S7 (a) Ir 4f XPS and (b) Ni 2p XPS spectra of Ni@IrNi-1, Ni@IrNi-2, and Ni@IrNi-3.

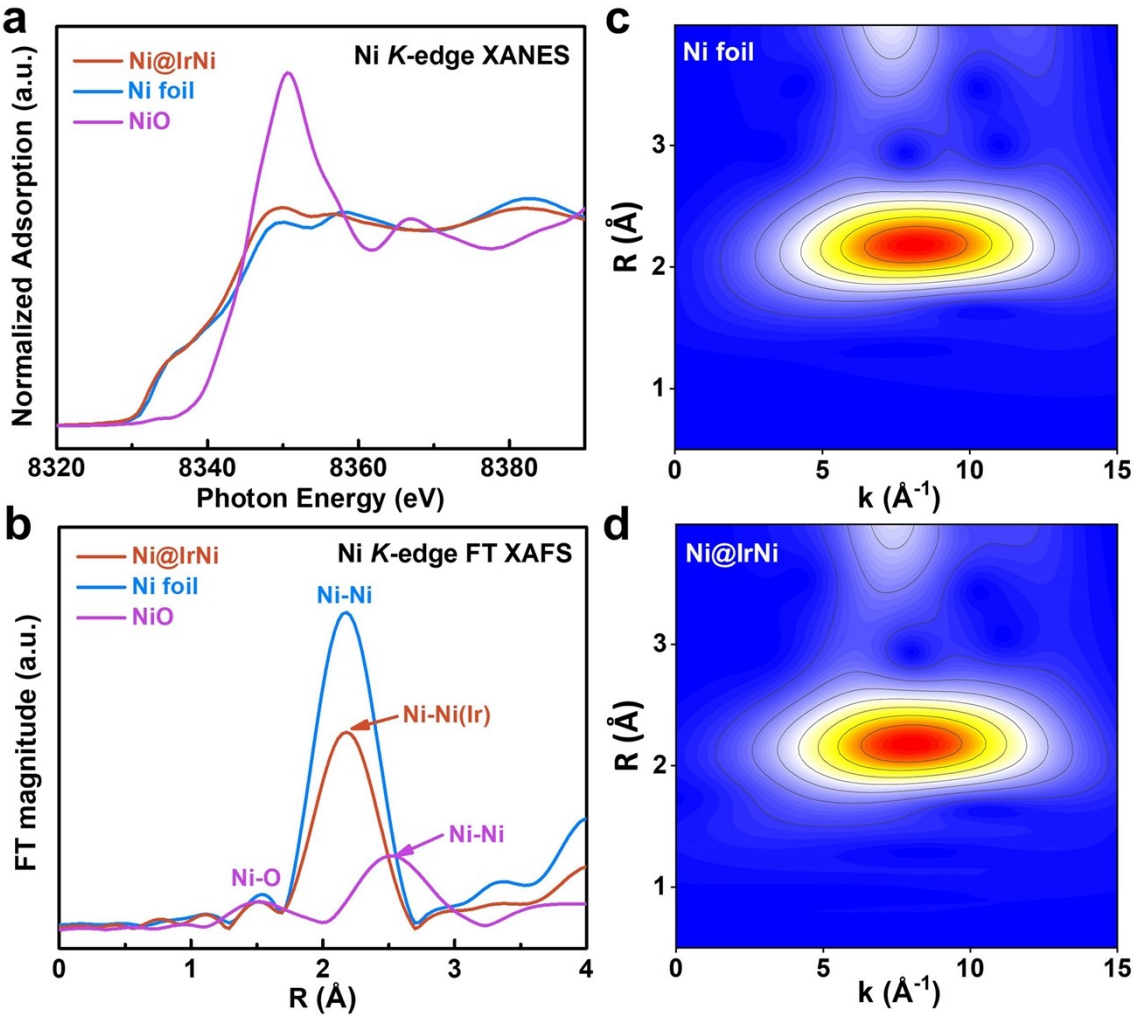

Fig. S8 (a) Ni K-edge XANES spectra and (b) EXAFS spectra of Ni@IrNi in comparison with the Ni foil and NiO references. (c,d) Wavelet transform of the EXAFS spectra of (c) Ir foil and (d) Ni@IrNi.

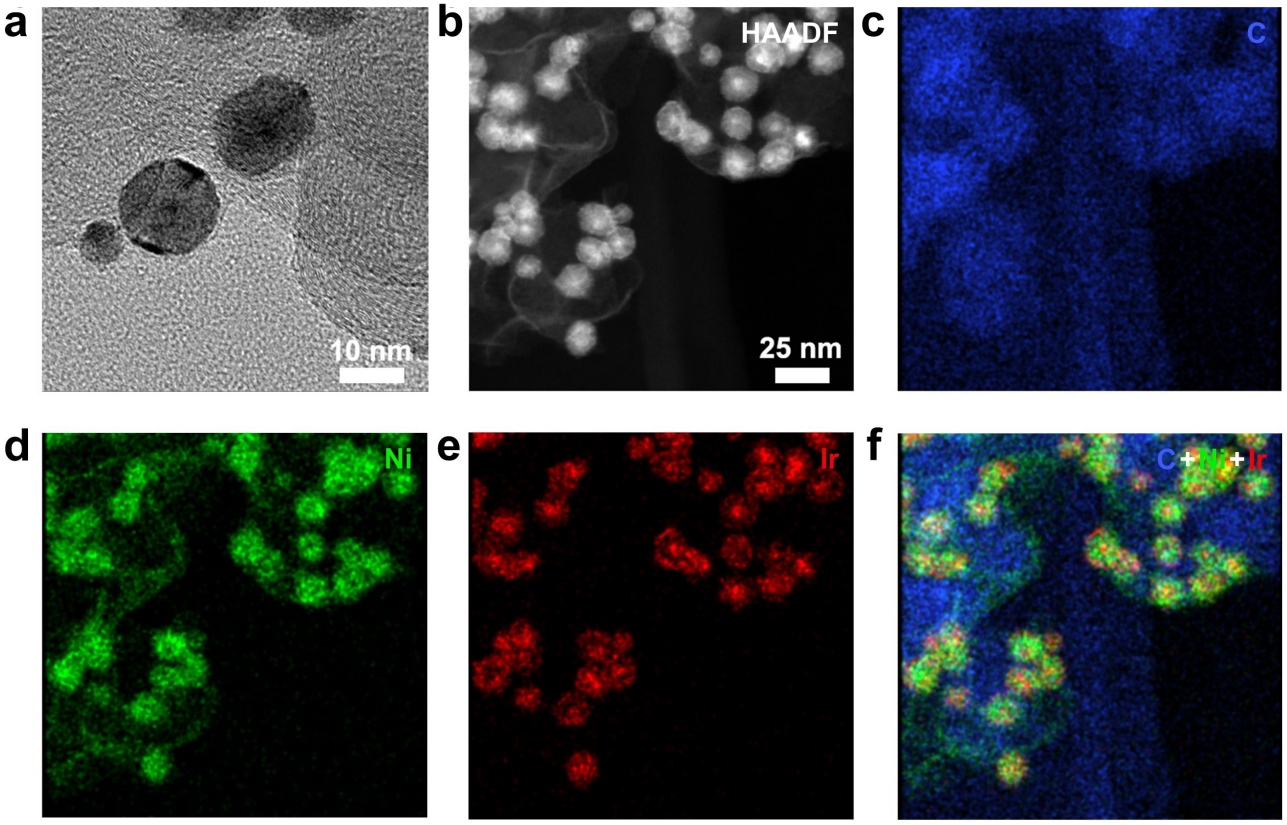

Fig. S9 (a) TEM image and (b) HAADF image of Ni@IrNi loaded on KB. (c-f) EDS elemental mapping of C, Ni and Ir in Ni@IrNi loaded on KB.

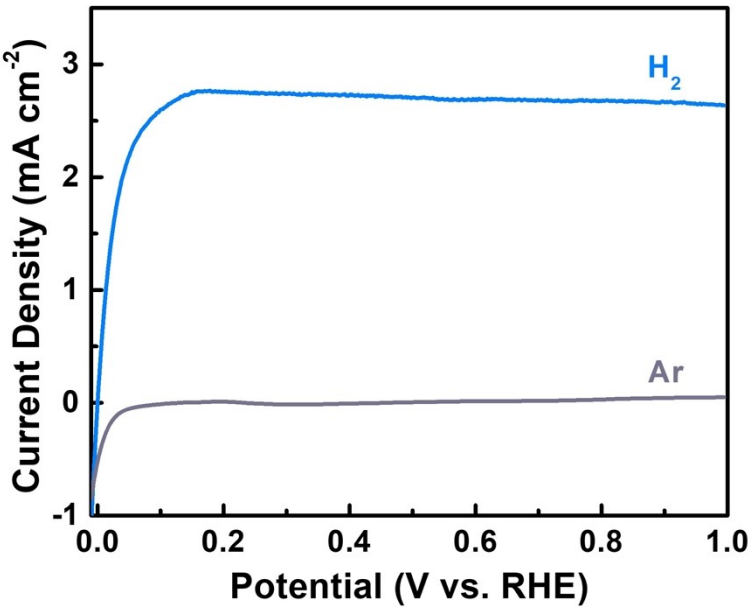

Fig. S10 Polarization curves of Ni@IrNi in H_2-saturated (blue) and Ar-saturated (grey) 0.1 M KOH at 1600 rpm.

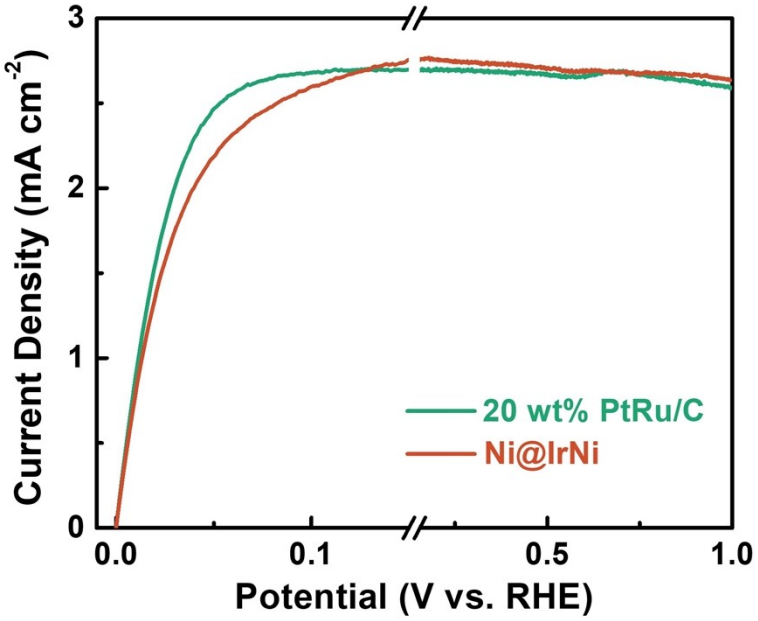

Fig. S11 HOR polarization curves of Ni@IrNi and 20 wt% PtRu/C at 1600 rpm in H_2-saturated 0.1 M KOH.

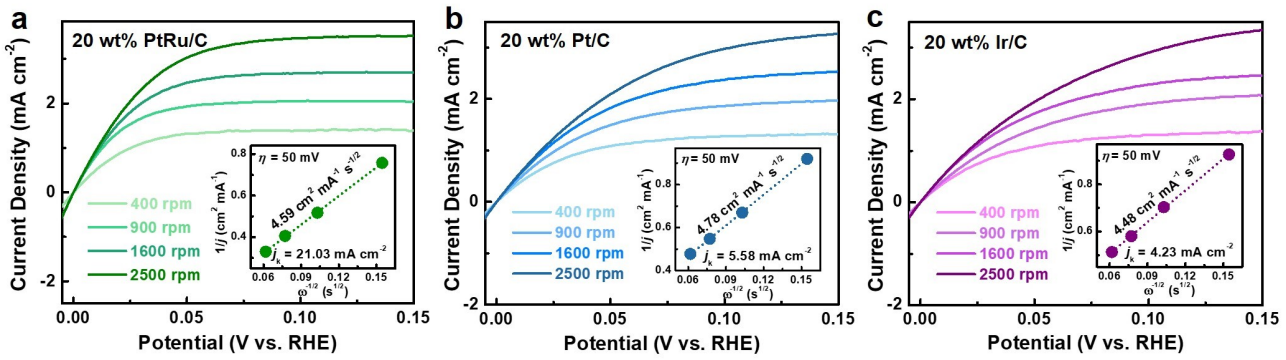

Fig. S12 Polarization curves of (a) 20 wt% PtRu/C, (b) 20 wt% Pt/C and (c) 20 wt% Ir/C at different electrode rotation speeds; the insets are the corresponding Koutecky–Levich plots at η = 50 mV.

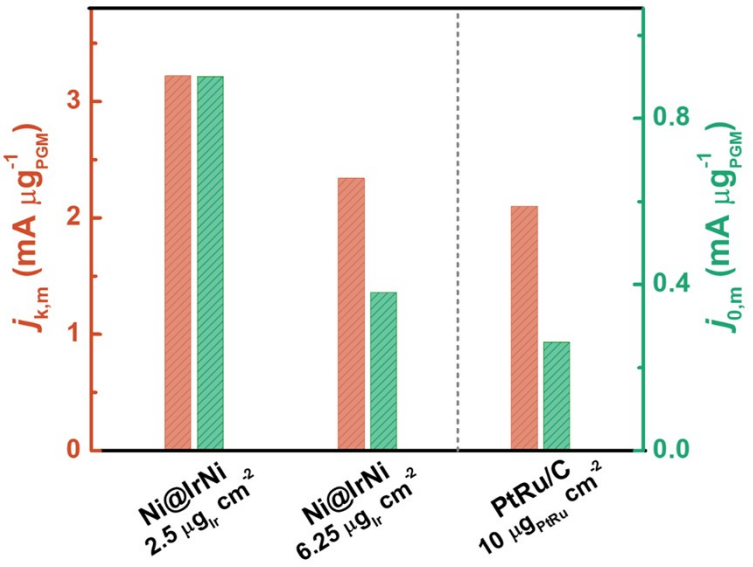

Fig. S13 Comparison of the mass-specific kinetic current $j_{k,m}$ and exchange current $j_{0,m}$ of 20 wt% PtRu/C and Ni@IrNi.

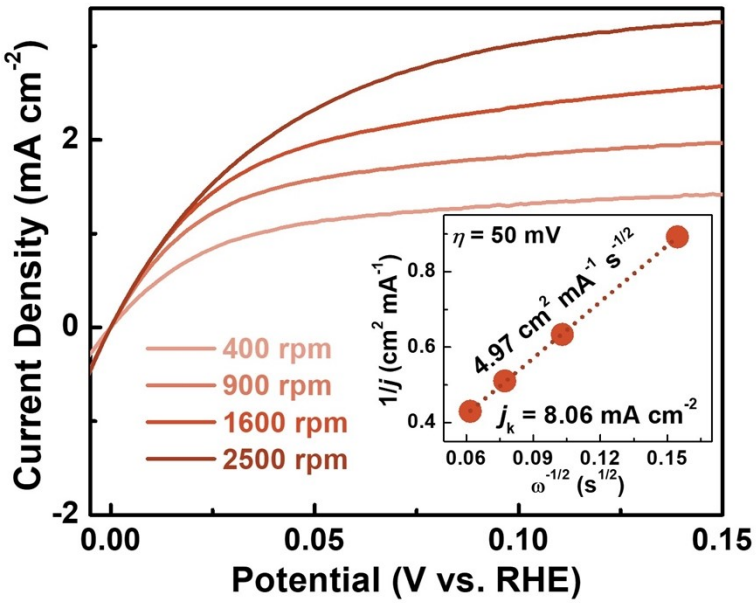

Fig. S14 Polarization curves of Ni@IrNi with an Ir loading of 2.5 μg cm^{-2} at different electrode rotation speeds, the inset is the corresponding Koutecky–Levich plot at η = 50 mV.

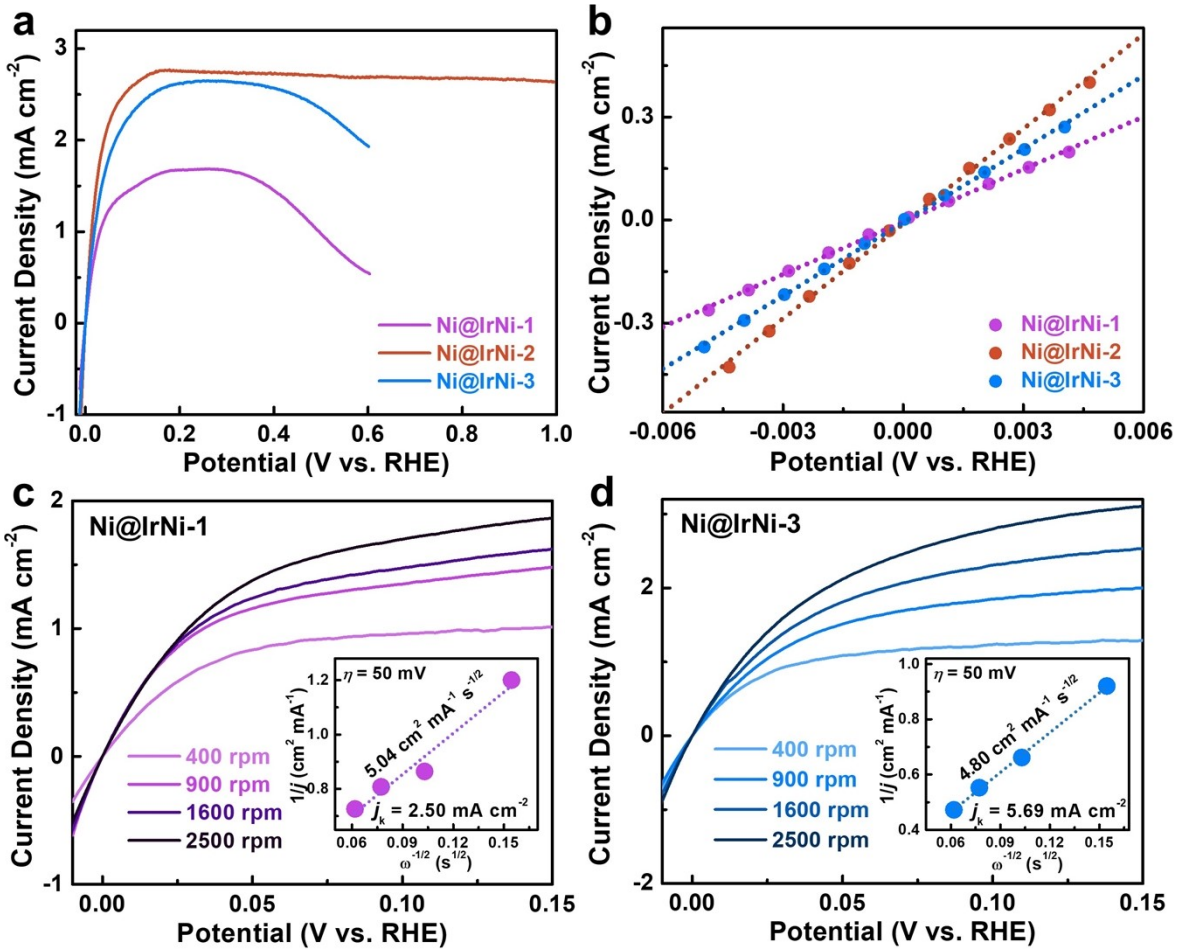

Fig. S15 (a) Comparison of the HOR polarization curves of Ni@IrNi-1, Ni@IrNi-2 and Ni@IrNi-3 in H_2-saturated 0.1 M KOH at 1600 rpm. (b) Micro-polarization curves of Ni@IrNi-1, Ni@IrNi-2 and Ni@IrNi-3 at 1600 rpm. (c,d) Polarization curves of (c) Ni@IrNi-1 and (d) Ni@IrNi-3 at different electrode rotation speeds; the insets are the corresponding Koutecky–Levich plot at η = 50 mV.

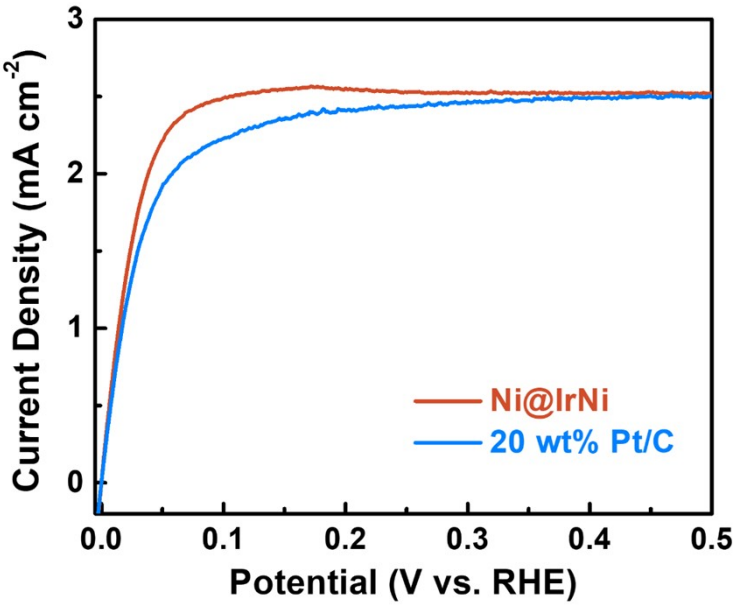

Fig. S16 HOR RDE polarization curves of Ni@IrNi and 20 wt% Pt/C in H_2-saturated 0.1 M PBS at 1600 rpm.

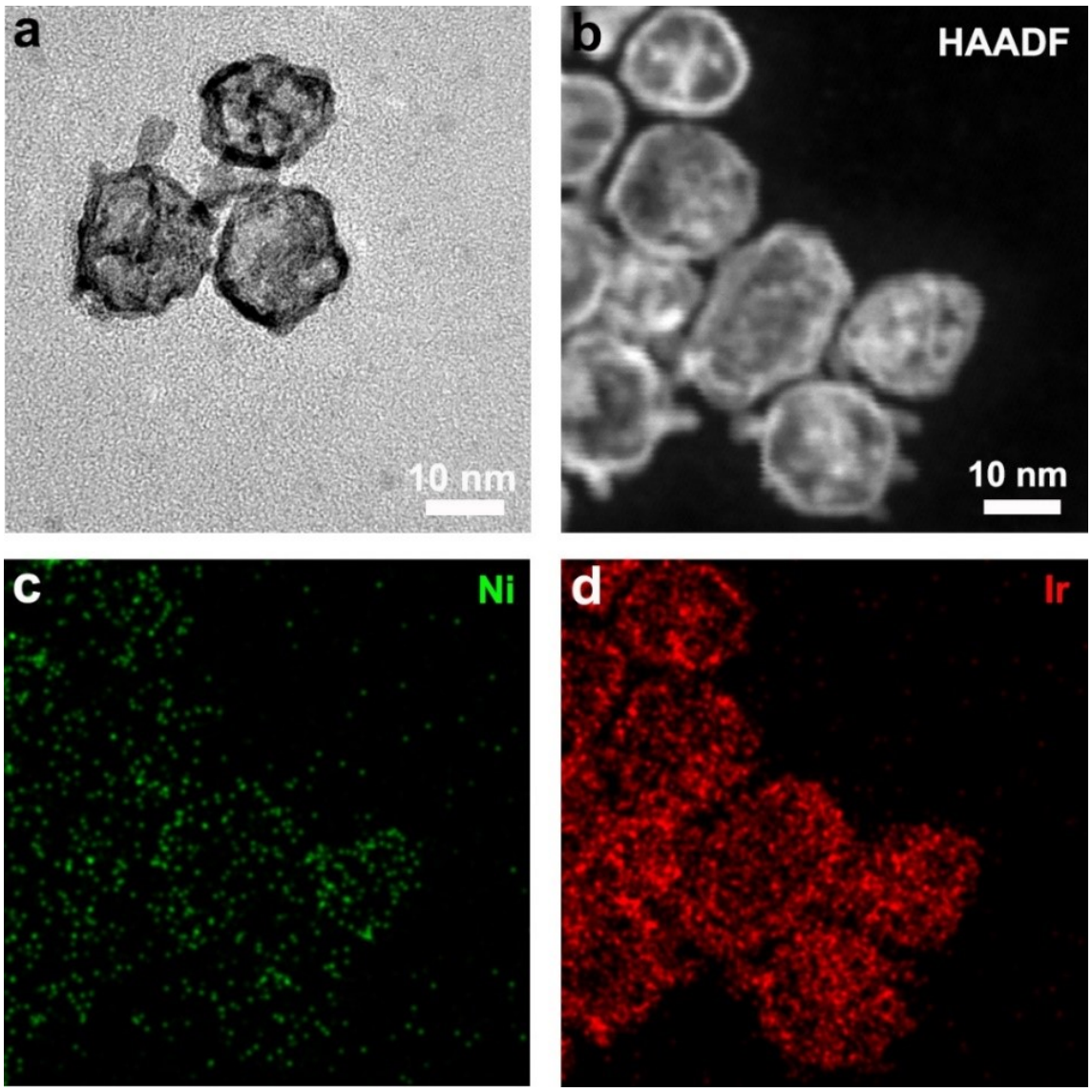

Fig. S17 (a) TEM image, (b) HAADF-STEM image and (c-d) EDS elemental mapping of e-Ni@IrNi.

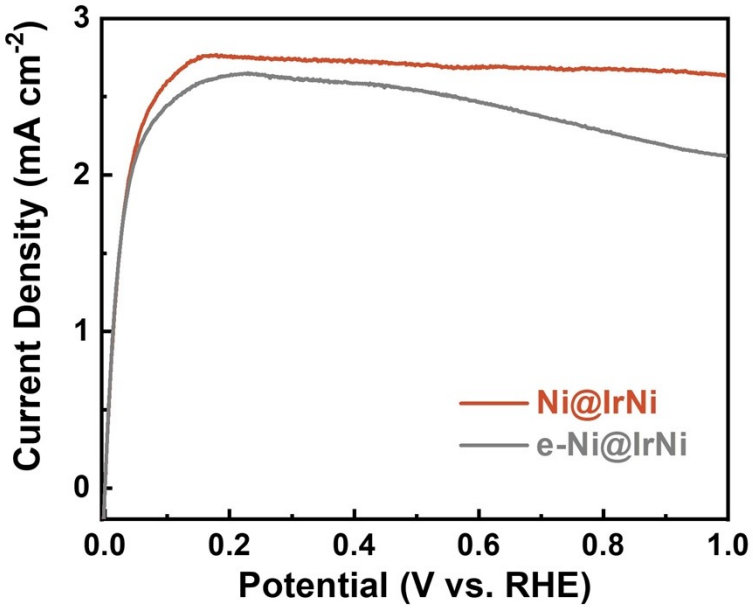

Fig. S18 HOR polarization curves of e-Ni@IrNi and Ni@IrNi catalysts with the same Ir loading of 6.25 μg cm^{-2} at 1600 rpm in H_2-saturated 0.1 M KOH.

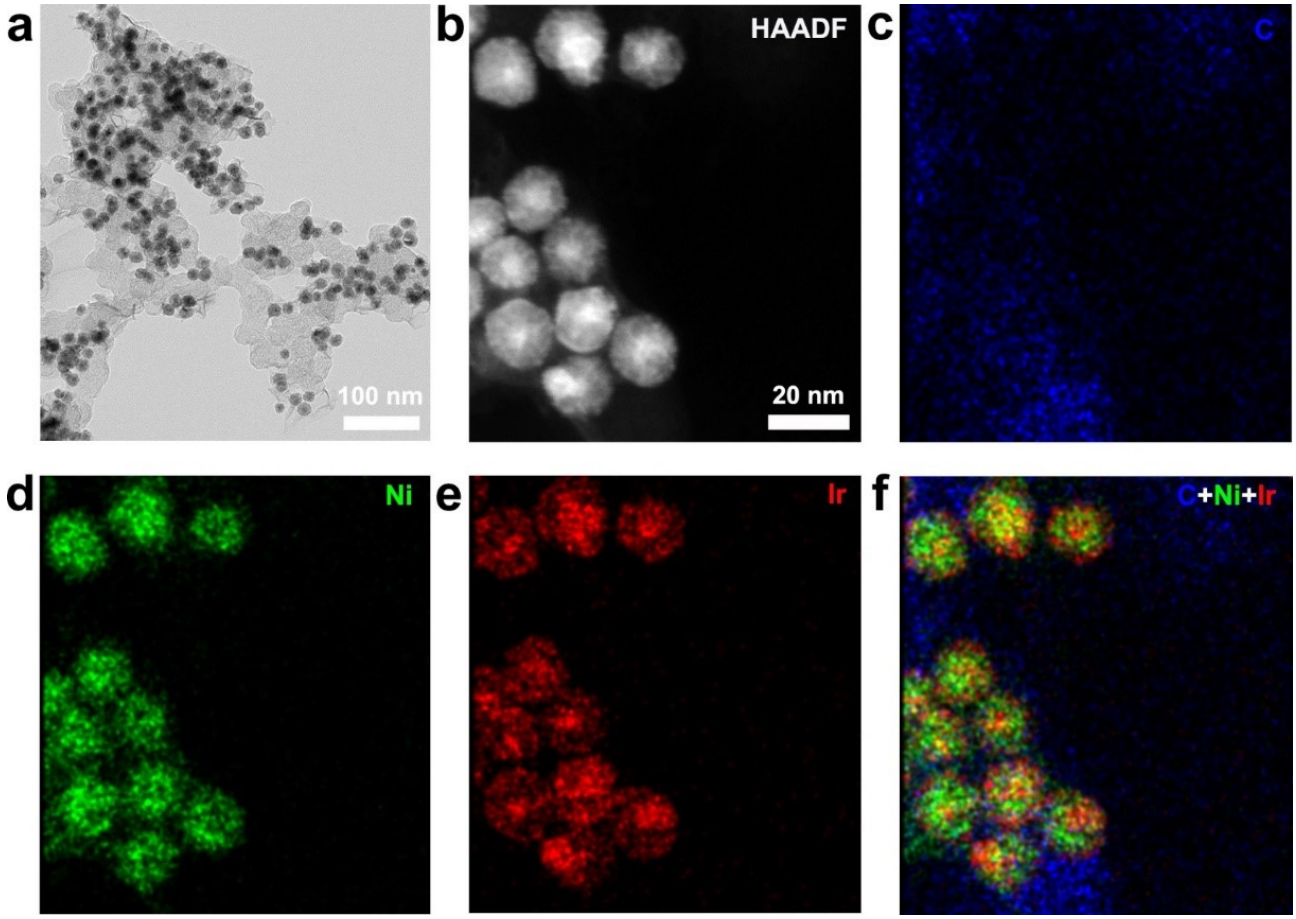

Fig. S19 (a) TEM image, (b) HAADF image and (c-f) EDS elemental mapping of Ni@IrNi loaded on KB after the chronoamperometry test.

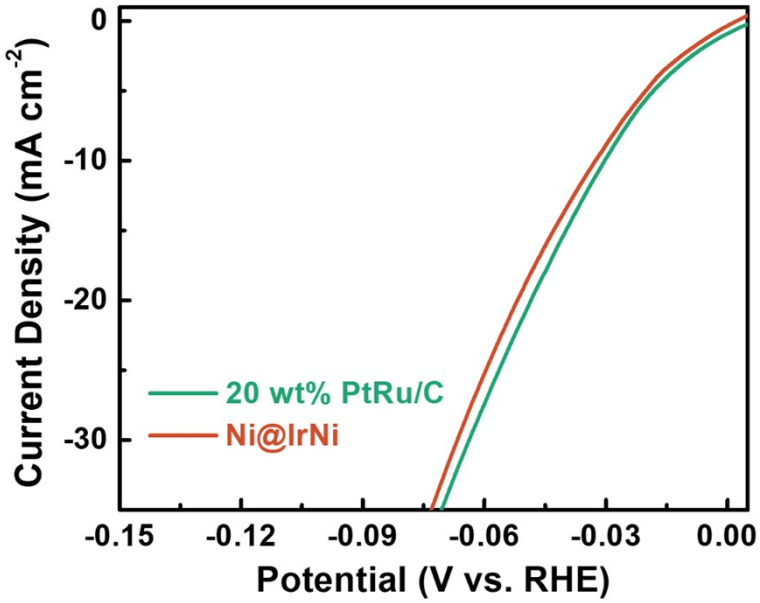

Fig. S20 HER polarization curves of Ni@IrNi and 20 wt% PtRu/C in 1 M KOH.

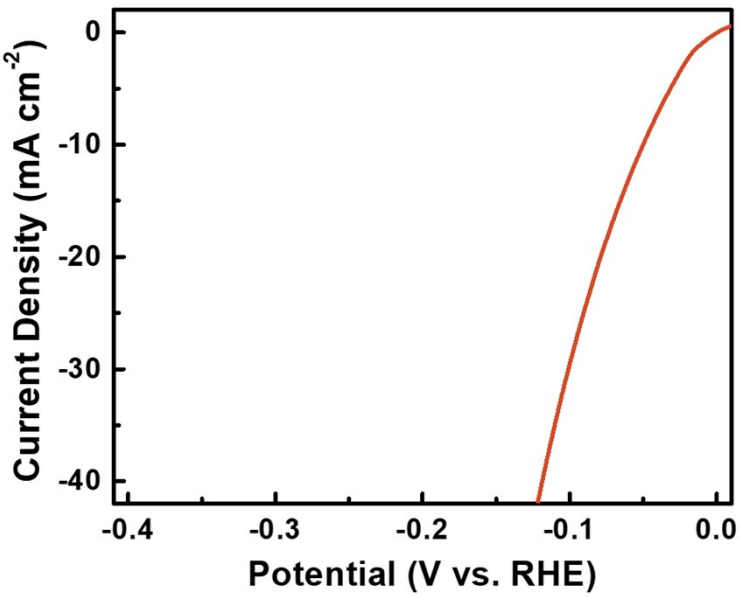

Fig. S21 HER polarization curve of Ni@IrNi with an Ir loading of 2.5 μg_{Ir} cm^{-2} in 1 M KOH.

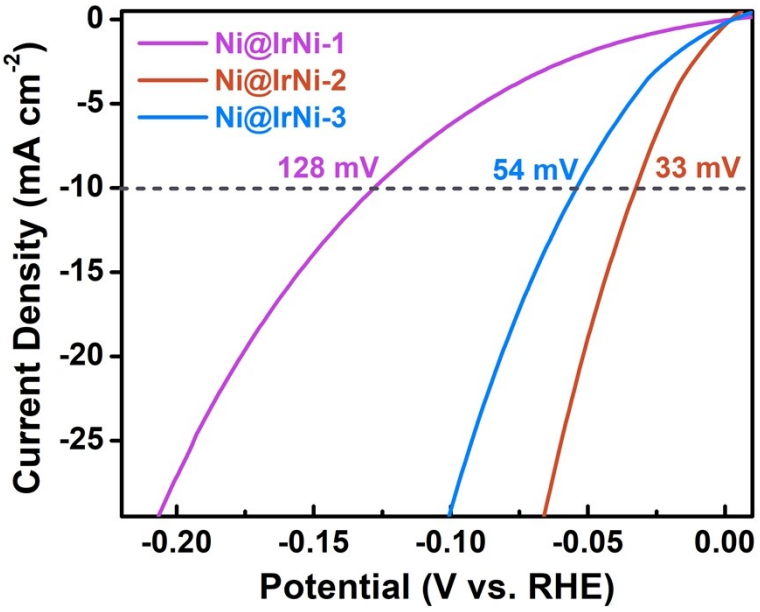

Fig. S22 HER polarization curves of Ni@IrNi-1, Ni@IrNi-2 and Ni@IrNi-3 in 1 M KOH.

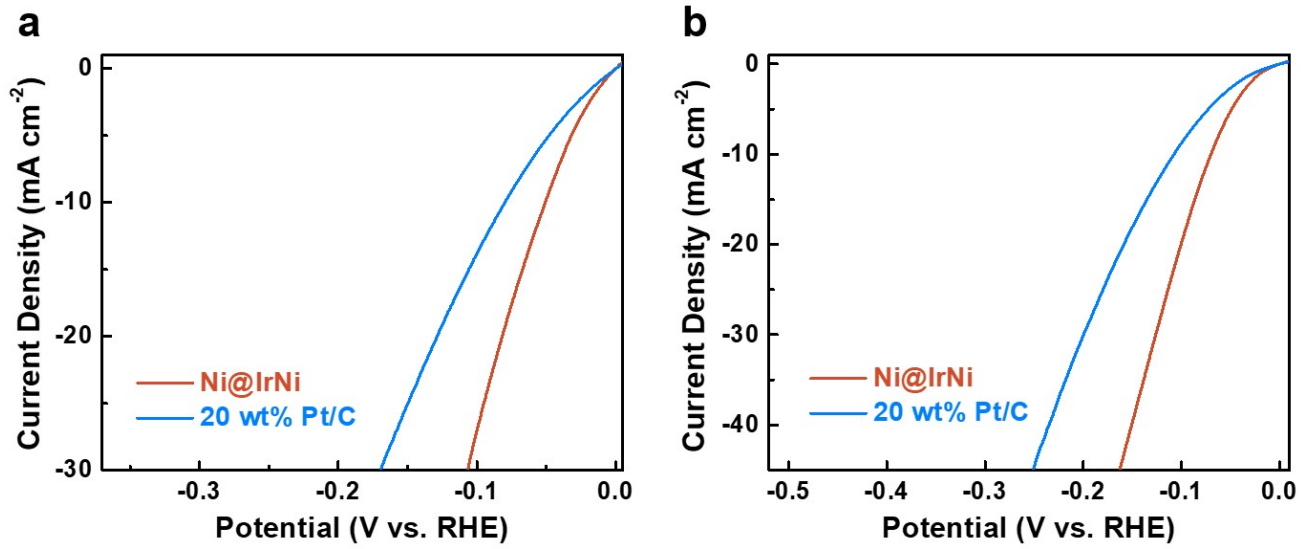

Fig. S23 HER polarization curves of Ni@IrNi and 20 wt% Pt/C in (a) 0.1 M KOH and (b) 1 M PBS.

Table S1 EXAFS fitting parameters for Ir–Ni and Ir–Ir paths in Ni@IrNi.

Sample	Path	S_0^2	CN	R(Å)	ΔE_0(eV)	$\sigma^2(10^{-3}$ Å$^2)$
Ni@IrNi	Ir-Ni	0.8	5.3	2.57	6.4	10.15
	Ir-Ir	0.8	4.6	2.67	6.4	3.53

Table S2 Comparison of the alkaline HOR activities of Ni@IrNi and other reported results.

Catalysts	$Loading_{PGM}$ μg cm^{-2}	j_k mA cm^{-2}	$j_{k,m}$ mA μg^{-1}	j_0 mA cm^{-2}	$j_{0,m}$ mA μg^{-1}	Reference
Ni@IrNi	6.25	14.54	2.34	2.38	0.381	This work
Ni@IrNi	2.50	8.06	3.22	2.25	0.901	This work
Ni@IrNi-1	3.45	2.50	0.72	1.32	0.383	This work
Ni@IrNi-3	8.58	5.69	0.66	1.84	0.215	This work
20 wt% PtRu/C	10	21.03	2.10	2.62	0.262	This work
20 wt% Pt/C	10	5.58	0.56	1.50	0.150	This work
20 wt% Ir/C	10	4.23	0.42	1.48	0.148	This work
Ru-Ru_2P	8.33	-	1.265	-	0.375	[23]
IrNi@Ir	10	-	1.12	1.16	0.116	[24]
IrNi@PdIr	17.43	16.82	0.965	0.209	0.012	[25]
Ru NP/PC	8.28	6.76	0.816	-	0.263	[26]
Ru_3Sn_7/C	5.536	-	0.658	-	0.291	[27]
O-RuNi@C	13.84	-	0.601	1.56	0.113	[28]
Ir/MoS_2	11.5	6.45	0.56	-	0.182	[14]
Ir ONAs	30	-	0.387	-	0.08	[12]
Ni-Ir(BCS)/G	31.8	-	0.33	2.86	0.09	[29]
RuNi/NC	25.25	5.59	0.221	2.66	0.105	[30]
Mo-Ru-2/C	6	-	1.86	3.02	0.503	[31]
Ir/Ni–NiO/CNT	29.16	-	1.59	2.04	0.070	[32]
Ir_2Ni_8/NHCSs	10	5.35	0.54	-	0.246	[33]
Ru/RuO_2-180	20	45.62	2.28	8.86	0.443	[34]
PtMo/MoO_x-1/C	9.43	-	3.19	-	0.406	[35]
PmPt@IrPd/C	5	-	-	-	0.743	[36]

Table S3 Comparison of the alkaline HER activities of Ni@IrNi and other reported results.

Catalysts	$Loading_{PGM}$ μg cm^{-2}	$\eta_{@\,j\,=\,10\ mA\ cm^{-2}}$ mV	Reference
Ni@IrNi	6.25	33	This work
Ni@IrNi-1	3.45	128	This work
Ni@IrNi-3	8.58	54	This work
20 wt% PtRu/C	10	30	This work
20 wt% Pt/C	10	72	This work
20 wt% Ir/C	10	80	This work
IrSi	-	38	[41]
NiVIr	608.8	41	[42]
Ir@N-G-750	11.5	43	[43]
Ru–MoS_2/CNT	263.3	50	[44]
RuP_2@NPC	233	52	[45]
$Ru_{0.33}$Se@TNA	59.6	57	[46]
Ru SAs–Ni_2P	11	57	[47]
Ir-NCNSs	7.6	125	[48]
Ru/Ni_2P@NPC	6.82	132	[49]

Table S4 Free energy corrections for gaseous species at T = 298.15 K.

Species	p	E_{elec}	ZPE	$-TS$	$\int Cp\mathrm{d}T$	G
	Pa	eV	eV	eV	eV	eV
H_2O	3167	-14.156	0.566	-0.673	0.103	-14.160
H_2	100000	-6.978	0.269	-0.403	0.090	-7.023